The demise of semidiurnal internal tides in the Equatorial Pacific: Incoherence or dissipation?

Maarten Buijsman[1], Brian K. Arbic[2], James G. Richman[3], and Luis Zamudio[3]

[1]University of Southern Mississippi, Stennis Space Center, MS
maarten.buijsman@usm.edu

[2]University of Michigan, Ann Arbor, MI
james.richman.ctr@nrlssc.navy.mil

[3]Florida State University, Tallahassee, FL
luis.zamudio.ctr@nrlssc.navy.mil

Abstract

The jets in the equatorial Pacific Ocean of a realistically-forced global circulation model yield a strong loss of phase coherence in semidiurnal internal tides that propagate equatorward from the French Polynesian islands and Hawaii. The loss of phase coherence is attributed to the time variability in the sheared background flow and stratification associated with the zonal jets. The incoherence due to background flow variability occurs on monthly time scales, whereas the incoherence due to stratification occurs on seasonal time scales. For time scales longer than a year the coherent energy flux approaches zero values at the equator, while the total flux, comprising the sum of the coherent, incoherent, and cross-term fluxes, remains non-zero. The 1/12.5° model simulation suggests that low-frequency jets do not noticeable enhance the dissipation of the internal tide, but merely decohere and scatter it. Thus, the model results presented here suggest that the apparent demise of coherent internal tides seen in satellite altimetry maps may be due to incoherence rather than dissipation.

Introduction

Internal gravity waves generated by barotropic tidal motions over underwater topography, also referred to as internal tides, fill the world's oceans (*Ray and Mitchum*, 1997; *Alford*, 2003; *Arbic et al.*, 2004). The internal tides that propagate long distances are mostly vertical low-mode waves (*Alford*, 2003), while the higher mode waves generally dissipate near their generation sites. Satellite altimetry of the ocean surface provides near-global coverage of low-mode internal tides (*Ray and Mitchum*, 1997; *Ray and Zaron*, 2011; *Shriver et al.*, 2012). Satellite altimeter maps show internal tides propagating across basins for thousands of kilometers. However, the equatorial Pacific ocean appears to be a barrier of sorts for internal tides. According to altimeter maps (see Figure 7a of *Shriver et al.* (2012)), neither beams that propagate southward from Hawaii or beams that propagate northward from the French Polynesian islands, cross the equatorial Pacific. This may imply that the equatorial zonal jets, and associated meridional gradients in stratification, cause a strong dissipation of the equatorward propagating internal tides. Another potential explanation for the apparent lack of internal tides at the equator is incoherence. The internal tide sea surface height signals are generally extracted from altimetry with a harmonic least-squares analysis (*Ray and Mitchum*, 1997; *Zhao et al.*, 2012; *Shriver et al.*, 2012), and only the part of the total signal that is coherent with the barotropic narrow-band tidal forcing is retained. The residual signal is defined as the incoherent or non-stationary part. A question that is addressed in this paper is how much of the apparent "dissipation" at the equator can be attributed to the internal tides becoming incoherent after passing through the equatorial Pacific jets, and thus being missed by the least squares analysis. Because of their $\mathcal{O}$(10 day) sampling times, satellite altimeters do not easily allow for estimation of the incoherent tide amplitude at a particular location in the ocean. In contrast, eddy-resolving numerical models with realistic tidal and atmospheric forcing allow for such local estimates (*Zaron and Egbert*, 2014; *Shriver*

et al., 2014).

Several mechanisms contribute to the incoherence of internal tides. First, the internal tide generation (barotropic to baroclinic conversion) may become incoherent with the tidal forcing due to local changes in stratification and/or remotely generated internal tides that arrive at irregular intervals (*Chavanne et al.*, 2014; *Nash et al.*, 2012b; *Kerry et al.*, 2014; *Kelly et al.*, 2015; *Pickering et al.*, 2015). After generation, the internal tides propagate through mesoscale flows, and the associated spatial and temporal variability in stratification, currents, and vorticity may cause time variable refraction of the internal gravity wave fields (*Rainville and Pinkel*, 2006; *Zaron and Egbert*, 2014; *Dunphy and Lamb*, 2014; *Ponte and Klein*, 2015). Hence, the internal tides become phase incoherent with the tidal forcing at a given location in the ocean. This leads us to the second and third questions to be discussed in this paper: what are the mechanisms of internal tide incoherence at the equator and on what time scales do they act?

In the remainder of this paper, we address these questions using output from the latest global HYbrid Coordinate Ocean Model (HYCOM) simulations with realistic tidal and atmospheric forcing. We first discuss the model and internal tide energy diagnostics. Next we diagnose the semidiurnal band-passed (total), the harmonically analyzed (coherent), and the residual (incoherent) energy fluxes radiating northward and southward from the French Polynesian islands. Finally, we discuss the mechanisms and time scales that underlie internal tide non-stationarity.

Methodology

Numerical Model

We utilize a recent version of HYCOM to study the incoherence of the the semidiurnal internal tide in the South Pacific. The simulation utilized here employs atmospheric forcing from the Navy Global Environmental Model (NAVGEM) (*Hogan et al.*, 2014) and geopotential tidal forcing for the five largest constituents (M_2, S_2, N_2, K_1 and O_1). The tidal forcing is augmented with a self-attraction and loading (SAL) term accounting for the load deformations and the self-gravitation of the tidally deformed ocean and solid earth (*Hendershott*, 1972). The simulation features 41 layers in the vertical direction and a nominal horizontal resolution of $1/12.5^\circ$ at the equator. The simulation is started from an initial state on 1 July 2011. Tidal forcing is initiated on 3 July 2011. Global three-dimensional fields are stored every hour for a one-year period from 1 October 2011 to 30 September 2012.

The simulation used here features several changes compared to our earlier HYCOM tidal simulations (*Shriver et al.*, 2012). We apply an Augmented State Ensemble Kalman Filter (ASEnKF) technique to reduce errors in the model's barotropic tidal sea surface elevations (*Ngodock et al.*, 2016). We use a tuned linear topographic internal wave drag scheme by *Jayne and St. Laurent* (2001) to account for unresolved high-mode internal wave generation and breaking (*Buijsman et al.*, 2015). Moreover, the model bathymetry is extended to include the ocean under the floating Antarctic ice shelves. These changes have greatly lowered the deep-water M_2 root-mean-square sea-surface error, from the 7.4 cm value in *Shriver et al.* (2012) to 2.6 cm in the simulation presented here.

Diagnostics

We diagnose the terms in the time-averaged and depth-integrated semidiurnal baroclinic energy equation (*Simmons et al.*, 2004; *Buijsman et al.*, 2014)

$$\nabla \cdot \mathbf{F} + D = C, \tag{1}$$

where $\mathbf{F} = (F_x, F_y)$ are the fluxes in the x (east-west) and y (north-south) directions, D is dissipation, and C is the barotropic to baroclinic energy conversion. D is computed as the residual of the flux divergence and conversion terms. We follow the approach by *Nash et al.*

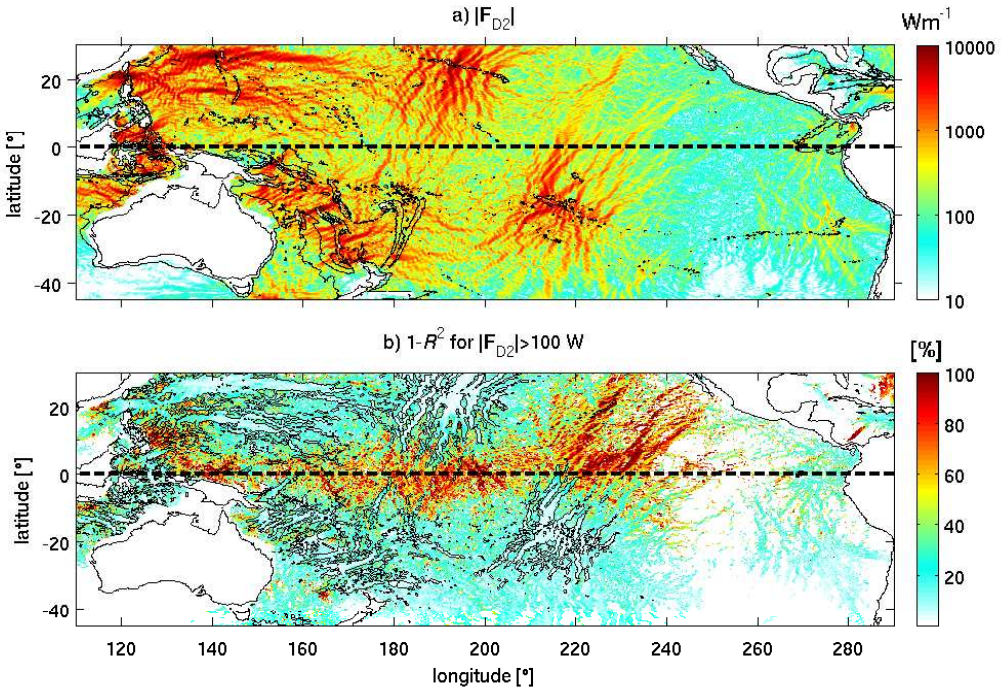

Figure 1: (a) The magnitude of the semidiurnal band-passed energy fluxes in the equatorial Pacific from HYCOM for the month of September 2012. In this month the flux incoherence near the equator is strong (Fig. 3a). Bathymetry is contoured at 0 and -2000 m. (b) The ratio of the sum of the incoherent and cross-term fluxes to the band-passed fluxes. Values coinciding with $|\mathbf{F}_{\mathrm{D2}}| < 100$ W m^{-1} are not shown. The black contours mark 1000 W m^{-1} of the band-passed fluxes. The equator is marked by the dashed black line.

(2012b) and *Pickering et al.* (2015) to compute the coherent and incoherent contributions to eq. (1). As a result of this decomposition, cross-terms appear that have contributions from both incoherent and coherent perturbation pressures and velocities. Although instantaneous values of the cross-term fluxes and conversion rates are non-zero, they disappear when averaged over periods of months to years.

We utilize the variance explained, or coefficient of determination (*Pickering et al.*, 2015)

$$R^2 = 1 - \frac{var(y-f)}{var(y)} \tag{2}$$

to quantify how much of the band-passed variance can be explained by the coherent signal, where y is the band-passed time series, f is the coherent time series, $var(x) = \sum_{i=1}^{n}(x_i - \overline{x})^2$ is the variance of time series x, n is the number of values in the time series, and $\overline{x}$ is the time-mean value. For the fluxes, we compute R^2 over the time series of the flux magnitudes $|\mathbf{F}(t)|$. We use $1 - R^2$ to quantify the variance of the incoherent relative to the band-passed signal.

Results

Equatorial Pacific

The Pacific ocean with its tall underwater ridges, such as Hawaii, the Mariana Islands, Luzon Strait, and the French Polynesian Islands is an important generator of radiating low-mode internal tides. The magnitudes of the semidiurnal band-passed fluxes computed over September 2012 are displayed in Fig. 1a. Although the analysis period is short, it is long enough for some energy fluxes to become incoherent once they pass through the equatorial region. The incoherence, $1-R^2$, is shown in Fig. 1b. As soon as the northward propagating internal tides from

the French Polynesian islands (20°S and 210°E) encounter the equator they become incoherent. In contrast, the southward propagating waves from the French Polynesian islands remain mostly coherent. The southward propagating internal tides from Hawaii (25°N and 190°E) also become incoherent after passing through the equatorial region. Another striking feature of Fig. 1b is that as soon as one moves away from the main beams, the incoherence increases. This means that the internal tides are most coherent in the beams and right near the generation sites, in accordance with findings by *Zaron and Egbert* (2014) and *Shriver et al.* (2014). If we compute $1 - R^2$ for an entire year, the patterns remain the same as in Fig. 1b, but the magnitudes are larger.

French Polynesia

In the following, we focus on the region to the north and south of the French Polynesian Islands, an isolated internal tide hotspot region (*Shriver et al.*, 2012). We compute time-mean energy flux and conversion terms every month and average them over 12 months (referred to as the "monthly mean") and for an entire year (referred to as the "annual mean"; Fig. 2), and then area-average them over the bins shown in Fig. 2e. In Fig. 2a the monthly-mean band-passed fluxes cannot be distinguished from the means computed for the annual time series (black solid and dashed curves). The band-passed energy fluxes decrease in magnitude away from the islands. This decay can be attributed to viscous, numeric, and wave drag dissipation (*Buijsman et al.*, 2016). The monthly-mean coherent fluxes show a faster decline compared with the band-passed fluxes to the north of the islands than they do to the south of the islands. The annual-mean coherent fluxes decline faster in magnitude away from the source than the monthly-mean fluxes (red dashed and solid curves). This inverse relation between coherent amplitude and record length has also been shown in *Nash et al.* (2012a), *Zhou et al.* (2015), and *Ansong et al.* (2015). The northward annual-mean coherent fluxes have become nearly zero at 5°N (see also Fig. 2e).

As the difference between the band-passed and coherent fluxes increases away from the source, the incoherent terms increase in magnitude, in particular along the northward beam (blue curves in Fig. 2b). For the monthly means a rapid increase occurs to the north of 5°S, while for the annual means this increase occurs at 13°S, i.e., closer to the source. After the initial rapid increase in the incoherent fluxes, the fluxes plateau. This may be because an approximate equilibrium state is reached and/or because there is some adulteration by more coherent internal tide beams from the Hawaiian island ridge. The cross-term fluxes decline in amplitude away from the source in Fig. 2b (cyan curves). In particular for the monthly mean fluxes, this decline is because the coherent pressure and velocity amplitudes, which are larger than the incoherent amplitudes, decline away from the generation sites. The annual-mean cross-term fluxes are nearly zero.

We show the annual-mean fraction of the energy flux that is dissipated per bin for band-passed and coherent fields in Fig. 2c. The monthly-mean fraction shows similar trends and is not plotted. At 25°S and 8°S, the fraction is impacted by enhanced conversion at deep topography causing larger dissipation rates and fluxes that oppose the main fluxes from the central ridge at 17°S. As with the band-passed fluxes, the band-passed fraction declines away from the central ridge. To the north of the Polynesian islands more energy is transferred more quickly to the incoherent fluxes than to the south, causing a larger divergence between the band-passed (dashed black line) and coherent fraction (dashed red line). While the coherent fraction peaks near the equator, the band-passed fraction essentially flatlines between 5°S and 5°N. This implies that the energy loss of the coherent internal tides north the Islands can be mainly attributed to incoherence scattering and not so much to dissipation in our 1/12.5° HYCOM simulations.

The variance of the band-passed fluxes explained by the coherent fluxes, R^2, is shown in Fig. 2d. Even for the monthly-mean R^2 values, the difference between the northward and southward internal tide beams is striking, with R^2 quickly dropping to values of about 20% in

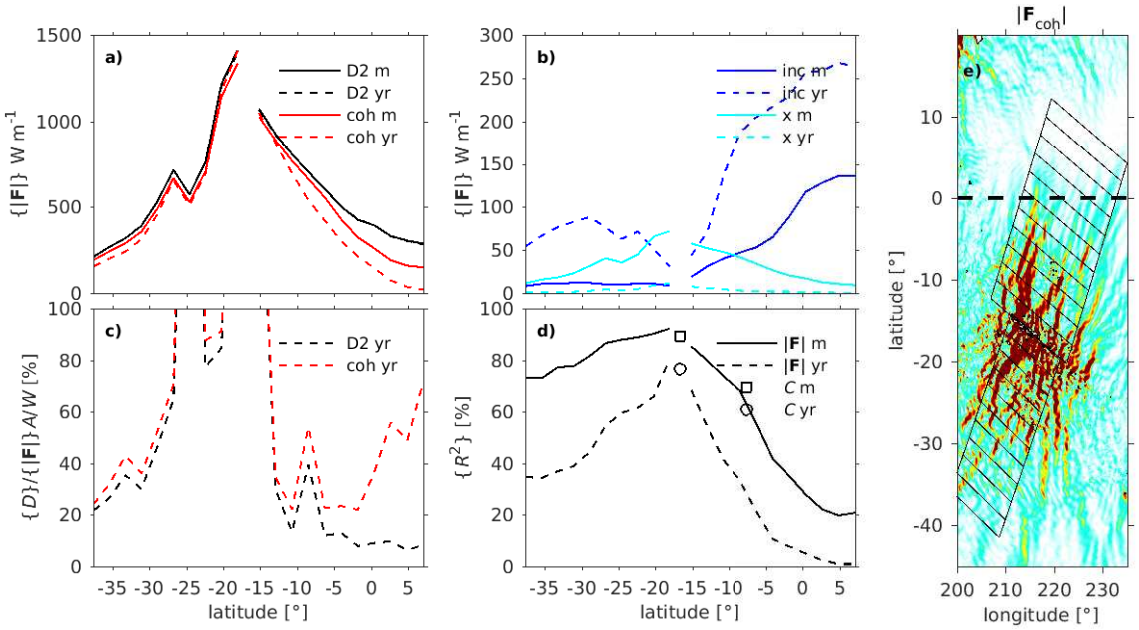

Figure 2: The magnitudes of the bin-averaged (a) and (b) semidiurnal fluxes radiating away from the French Polynesian islands, (c) the fraction of the bin-width integrated absolute flux that is lost to the area-integrated dissipation, and (d) variance of the band-passed fluxes and conversion explained by the coherent fluxes (curves) and conversion (symbols). The bins are shown on top of the annual-mean coherent fluxes in (e). The band-passed, coherent, incoherent, and cross terms are denoted by 'D2', 'coh', 'inc', and 'x'. The annual means over the monthly means are labeled with 'm' and the means computed over the one-year-long time series are labeled with 'yr'.

the north. The R^2 values are further reduced in the annual means. At 5°N the annual mean R^2 has dropped to near-zero values, indicating no phase coherence. The R^2 values of the monthly-mean and annual conversion rates at the Islands are similar to the near-field fluxes (Fig. 2d). This implies that the conversion is minimally affected by remotely generated internal tides and background variability.

Discussion

In a general circulation model forced by both atmospheric fields and the astronomical tidal potential, there is a striking loss of coherence in the propagating semidiurnal internal tides as they pass through the equatorial Pacific Ocean. We attribute the loss of coherence of the equatorward beams to the time variability of the equatorial jets. In the jets zonal surface velocities are $\mathcal{O}(1\ \mathrm{ms}^{-1})$ and vary in time by $\pm \sim 0.5\ \mathrm{ms}^{-1}$. The north-south extent of the jets is about 1700 km (5°S—10°N), and they reach about 300 deep. Note that the jets' location is offset to the north of the equator, consistent with the greater amount of incoherence seen in the northern hemisphere noted earlier.

To further investigate the causes of the incoherence, we follow a similar approach as outlined by *Zaron and Egbert* (2014). They attribute the loss of coherence of an internal tide to 1) refraction due to the time-varying background stratification, 2) Doppler shifting or advection by the time-varying subtidal current, and 3) refraction due to time-varying background relative vorticity. Similar to *Zaron and Egbert* (2014) we find that the former two are more important than the latter in the equatorial region.

Our approach differs from *Zaron and Egbert* (2014) as we solve the Taylor Goldstein equation (*Smyth et al.*, 2010) to account for depth-dependent stratification and vertically sheared horizontal subtidal flow. First we compute the two-day mean velocity and stratification fields

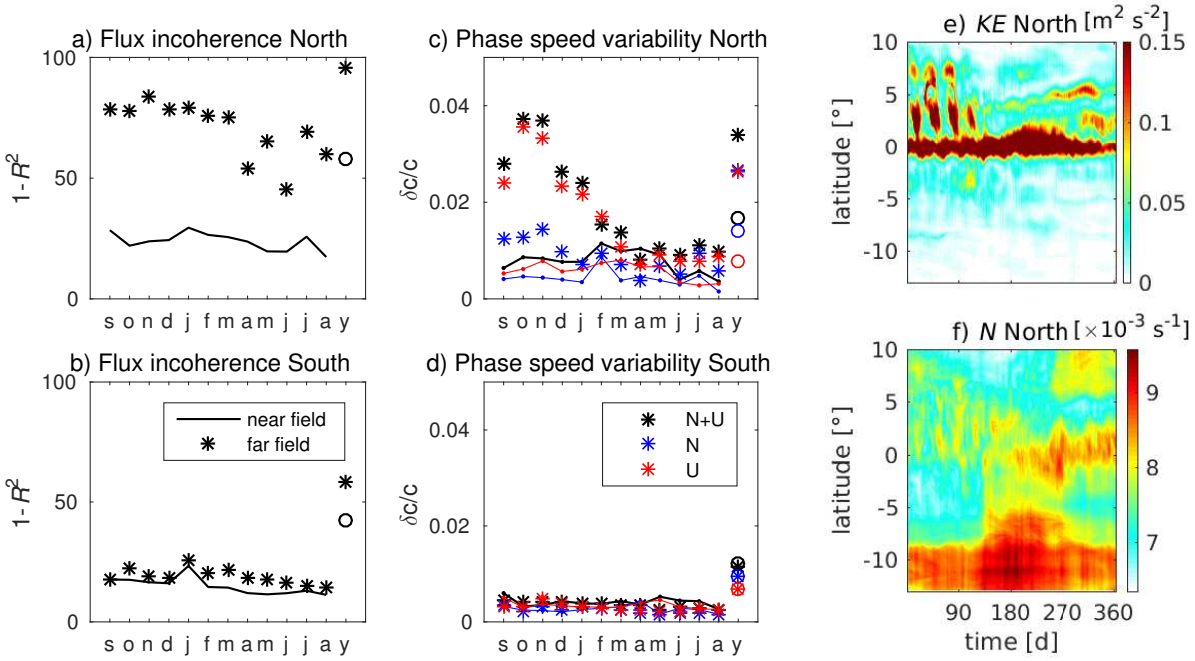

Figure 3: The relation between flux incoherence (a-b) and possible causes (c-f). The monthly-mean (months s-a) and annual-mean (y) incoherence along (a) a transect north and (b) a transect south of the Polynesian Islands. The monthly-mean and annual-mean variance of the normalized phase-speed as a function of background velocity and stratification ($N+U$), stratification (N), and velocity (U) along (c) the northern and (d) the southern transect. The transects coincide with the western boundary of the bins in Fig. 2e. The nearfield (lines) is bounded by 13°S-5°S and 30°S-13°S and the farfield (symbols) by 5°S-10°N and 45°S-30°S. The two-daily mean (e) kinetic energy and (f) stratification averaged over the surface 500 m for the northern transect.

along transects to the north and south of the French Polynesian Islands. The transects are aligned with major internal tide beams and coincide with the western boundary of the bins in Fig. 2e. For each two-day period we compute the phase velocity for three cases: 1) time-varying stratification and shear flow, 2) time-varying stratification only, and 3) time-varying shear flow with a time-mean stratification. The normalized monthly-mean variance and annual-mean variance of the phase speed for the near and farfield along the two transects are in Fig. 3c and d. Along the northern transect, the farfield region coincides with the equatorial jets.

The monthly-mean variance in the phase speed due to shear flow and stratification (black stars) north of the equator is mainly attributed to the variance in the shear flow (red stars) Fig. 3c. This variance is the strongest for the period September-January and clearly coincides with variability in large surface kinetic energy associated with the jets in Fig. 3e. In contrast, on an annual time scale (label y in Fig. 3a-d), the phase speed variance is equally attributed to shear flow and stratification, or stratification variance is larger than shear flow variance. Fig. 3f shows that the seasonal changes in stratification are larger than changes on monthly time scales. Along the southern transect, the phase speed variance is much smaller than to the north, and the variance in the farfield is similar to the variance in the nearfield.

The incoherence of the semidiurnal energy fluxes in Fig. 3a and b is in general agreement with the phase-speed variance in Fig. 3c and d. The incoherence and phase-speed variance are both large in the farfield and small in the nearfield along the northern transect and small in the near- and farfield along the southern transect. Moreover the annual-mean incoherence and variance are larger than the annual-mean of the monthly-mean values. There is partial agreement between the incoherence and the phase speed variance regarding their seasonal variability in the equatorial region (Fig. 3a and c). Both the incoherence and phase-speed variance are large in the first half and small in the second half of the year. However, the range of the variance is

larger and its seasonal peak narrower than the incoherence. This difference may be attributed to the relative simplicity of our Taylor Goldstein approach.

In agreement with altimetry observations of semidiurnal internal tide surface amplitudes (*Shriver et al.*, 2012), we find that annual-mean coherent internal tides are quite weak at the equator, i.e. their energy flux is near zero (Fig. 2e). The equatorial jets between 5°S—5°N do not cause a noticeable increase in the band-passed dissipation of the semidiurnal internal tide in the 1/12.5° HYCOM simulations (Fig. 2c). Hence, we conclude that in these 1/12.5° resolution simulations the jets dramatically decohere the internal tides instead of dissipating them. Our results are in agreement with model studies by *Dunphy and Lamb* (2014) and *Ponte and Klein* (2015), who show that mesoscale structures such as eddies and jets can decohere, refract, and scatter the internal tides. However, analysis of higher-resolution simulations is needed to be more conclusive about the effect of the jets on internal tide dissipation. Higher resolution simulations may include wave-mean flow interactions that facilitate internal wave breaking (*Bühler and McIntyre*, 2005).

Acknowledgements

M.C Buijsman acknowledges support from the Office of Naval Research under awards ONRDC32025354 and ONRDC38645449. J.G. Richman and L. Zamudio thank ONR for supporting this work under program element 0602435N. B.K. Arbic thanks ONR for support under grant numbers N00014-11-1-0487 and N00014-15-1-2288. This work was supported in part by a grant of computer time from the DOD High Performance Computing Modernization Program at the Navy DSRC.

References

Alford, M. H. (2003), Redistribution of energy available for ocean mixing by long-range propagation of internal waves, *Nature*, *423*, 159–162.

Ansong, J. K., B. K. Arbic, M. C. Buijsman, J. G. Richman, J. F. Shriver, and A. J. Wallcraft (2015), Indirect evidence for substantial damping of low-mode internal tides in the open ocean, *J. Geophys. Res.*, doi:10.1002/2015JC010998.

Arbic, B. K., S. T. Garner, R. W. Hallberg, and H. L. Simmons (2004), The accuracy of surface elevations in forward global barotropic and baroclinic tide models, *Deep-Sea Res. II*, *51*, 3069–3101.

Bühler, O., and M. E. McIntyre (2005), Wave capture and wave-vortex duality, *J. Fluid Mech.*, *534*, 67–95.

Buijsman, M., J. K. Ansong, B. K. Arbic, J. G. Richman, J. F. Shriver, P. G. Timko, A. J. Wallcraft, C. Whalen, and Z. Zhao (2016), Impact of internal wave drag on the semidiurnal energy balance in a global ocean circulation model, *J. Phys. Oceanogr.*, *46*, 1399–1419.

Buijsman, M. C., J. M. Klymak, S. Legg, M. H. Alford, D. Farmer, J. A. MacKinnon, J. D. Nash, J.-H. Park, A. Pickering, and H. Simmons (2014), Three Dimensional Double Ridge Internal Tide Resonance in Luzon Strait, *J. Phys. Oceanogr.*, *44*, 850–869.

Buijsman, M. C., B. K. Arbic, J. A. M. Green, R. W. Helber, J. G. Richman, J. F. Shriver, P. G. Timko, and A. J. Wallcraft (2015), Optimizing Internal Wave Drag in a Forward Barotropic Model with Semidiurnal Tides, *Ocean Modell.*, *85*, 42–55.

Chavanne, C., P. Flament, D. Luther, and K.-W. Gurgel (2014), The surface expression of semidiurnal internal tides near a strong source at Hawaii. Part II: Interactions with mesoscale currents, *J. Phys. Oceanogr.*, *40*, 1180–1200.

Dunphy, M., and K. G. Lamb (2014), Focusing and vertical mode scattering of the first mode internal tide by mesoscale eddy interaction, *J. Geophys. Res.*, *119*, 523–536.

Hendershott, M. C. (1972), The effects of solid earth deformation on global ocean tides., *Geophys. J. Roy. Astr. Soc.*, *29*, 389–402.

Hogan, T. F., M. Liu, J. A. Ridout, M. S. Peng, T. R. Whitcomb, B. C. Ruston, C. A. Reynolds, S. D. Eckermann, J. R. Moskaitis, N. L. Baker, J. P. McCormack, K. C. Viner, J. G. McLay, M. K. Flatau, L. Xu, C. Chen, and S. W. Chang (2014), The Navy Global Environmental Model, *Oceanography*, *27*, 116–125.

Jayne, S. R., and L. C. St. Laurent (2001), Parameterizing tidal dissipation over rough topography, *Geophys. Res. Lett.*, *28*, 811–814.

Kelly, S. M., N. L. Jones, G. N. Ivey, and R. J. Lowe (2015), Internal-tide spectroscopy and prediction in the Timor Sea, *J. Phys. Oceanogr.*, *45*, 64–83.

Kerry, C., B. Powell, and G. Carter (2014), The impact of subtidal circulation on internal-tide generation and propagation in the Philippine Sea, *J. Phys. Oceanogr.*, *44*, 1386–1405.

Nash, J., E. Shroyer, S. Kelly, M. Inall, T. Duda, M. Levine, N. Jones, and R. Musgrave (2012a), Are any coastal internal tides predictable?, *Oceanography*, *25*, 80–95.

Nash, J. D., S. M. Kelly, E. L. Shroyer, J. N. Moum, and T. F. Duda (2012b), The unpredictable nature of internal tides on continental shelves, *J. Phys. Oceanogr.*, *42*, 1981–2000.

Ngodock, H. E., I. Souopgui, A. J. Wallcraft, J. G. Richman, J. F. Shriver, and B. K. Arbic (2016), On improving the accuracy of the barotropic tides embedded in a high-resolution global ocean circulation model, *Ocean Modell.*, *97*, 16–26.

Pickering, A., M. Alford, J. Nash, L. Rainville, M. Buijsman, D. Ko, and B. Lim (2015), Structure and Variability of Internal Tides in Luzon Strait, *J. Phys. Oceanogr.*, *45*, 1574–1594.

Ponte, A. L., and P. Klein (2015), Incoherent signature of internal tides on sea level in idealized numerical simulations, *Geophys. Res. Lett.*, *42*, 1520–1526, doi:10.1002/2014GL062583.

Rainville, L., and R. Pinkel (2006), Propagation of low-mode internal waves through the ocean, *J. Phys. Oceanogr.*, *36*, 1220–1236.

Ray, R. D., and G. T. Mitchum (1997), Surface manifestation of internal tides in the deep ocean: observations from altimetry and island gauges, *Prog. Oceanogr.*, *40*, 135–162.

Ray, R. D., and E. D. Zaron (2011), Non-stationary internal tides observed with satellite altimetry, *Geophys. Res. Lett.*, *38*, L17609, doi:10.1029/2011GL048617.

Shriver, J. F., B. K. Arbic, J. G. Richman, R. D. Ray, E. J. Metzger, A. J. Wallcraft, and P. G. Timko (2012), An evaluation of the barotropic and internal tides in a high resolution global ocean circulation model, *J. Geophys. Res.*, *117*, C10024, doi:10.1029/2012JC008170.

Shriver, J. F., J. G. Richman, and B. K. Arbic (2014), How stationary are the internal tides in a high-resolution global ocean circulation model?, *J. Geophys. Res.*, *119*, doi:10.1002/2013JC009423.

Simmons, H. L., R. W. Hallberg, and B. K. Arbic (2004), Internal wave generation in a global baroclinic tide model, *Deep-Sea Res. II*, *51*, 3043–3068.

Smyth, W., J. Moum, and J. Nash (2010), Narrowband, high-frequency oscillations at the equator. Part II: Properties of shear instabilities, *J. Phys. Oceanogr.*, *41*, 412–428.

Zaron, E. D., and G. D. Egbert (2014), Time-variable refraction of the internal tide at the Hawaiian Ridge, *J. Phys. Oceanogr.*, *44*, 538–557.

Zhao, Z., M. Alford, and J. Girton (2012), Mapping low-mode internal tides from multisatellite altimetry, *Oceanography*, *25*, 42–51.

Zhou, X.-H., D.-P. Wang, and D. Chen (2015), Validating satellite altimeter measurements of internal tides with long-term TAO/TRITON buoy observations at 2°S-156°E, *Geophys. Res. Lett.*, *42*, 4040–4046, doi:10.1002/2015GL063669.